Desalination 628 (2026) 120111

Contents lists available at ScienceDirect

Desalination

journal homepage: www.elsevier.com/locate/desal

A compact photovoltaic–thermal (PV/T) desalination system: Device development and performance optimization

Lihao Yuan [a,1], Zhiheng Qiu [a,1], Omar AlAli [b], Ronghui Qi [c], Mengying Li [a,*]

[a] Department of Mechanical Engineering , The Hong Kong Polytechnic University, Hong Kong Special Administrative Region
[b] Department of Mechanical Engineering, College of Engineering and Petroleum, Kuwait University, Kuwait
[c] School of Chemistry and Chemical Engineering, South China University of Technology, Guangzhou, China

HIGHLIGHTS

- Develop a compact PV/T desalination system to co-generate electricity and freshwater.
- Optimize the device structure and materials to improve overall performance.
- Device inclination angles has no significant effect on freshwater yield under constant irradiance.
- Outdoor sun-tracking mode increased daily freshwater yield by 53.8% compared with fixed-orientation mode.

ARTICLE INFO

Keywords:
Photovoltaic–thermal
Solar desalination
Interfacial evaporation
Membrane distillation
Design and operational optimization

ABSTRACT

Utilizing waste heat from photovoltaic (PV) panels for desalination offers a practical pathway for cascading energy use and addressing the energy–water nexus. A compact photovoltaic–thermal (PV/T) interfacial evaporation desalination system was developed that integrates capillary-driven evaporation, membrane distillation, and condensation directly into the PV panel assembly. The system harnesses the waste heat from the PV backsheet (typically accounting for 80%–85% of incident solar energy) to drive water evaporation through a cotton fabric wick, while a distillation membrane separates vapor from brine. A SiO_2-nanocoated aluminum condenser with high hydrophobicity (contact angle 107.9°) is equipped with sea–island fiber guides and dual bottom outlets, achieving a freshwater collection efficiency of over 90%. Indoor experiments at three inclination angles (5°, 15°, and 25°) under controlled irradiance conditions (400–1000 W/m^2) show that the inclination angle has no significant effect on freshwater productivity under constant irradiance. Outdoor testing in Hong Kong at a fixed 22° inclination yielded a cumulative daily freshwater production of 1.73 L/m^2 and a daily GOR of 0.348. Sun-tracking mode, achieved through manual surface azimuthal adjustments every 10 min, increased incident irradiance by 23.5%, GOR by 5%, and the daily water yield by 53.8% to 2.66 L/m^2. This compact, cost-effective system offers a practical solution for distributed solar desalination, particularly in water-scarce, sun-rich regions, and demonstrates the potential for efficient utilization of solar energy.

1. Introduction

Access to water and energy remains a critical challenge in remote and distributed settings worldwide. More than half of the global population is projected to face severe water stress by 2100 [1–4], while billions lack reliable electricity access [5]. These challenges often coincide geographically, as water-scarce regions frequently receive abundant solar irradiation [6]. Standalone desalination systems and photovoltaic installations address these needs independently, but doing so requires separate infrastructure, land area, and capital investment. Integrated systems that simultaneously provide electricity and freshwater from a single solar installation offer a more practical solution for decentralized applications in resource-constrained regions.

Photovoltaic installations have expanded rapidly, with global capacity reaching 1.6 TW by 2023 [7]. PV panels operate at relatively low conversion efficiency, transforming only 15%–20% of incident solar energy into electricity [8]. The remaining 80%–85% accumulates as waste heat, elevating panel temperatures to 60–80°C during operation [9]. This thermal energy is typically dissipated to the environment

---

[*] Corresponding author.
E-mail address: mengying.li@polyu.edu.hk (M. Li).
[1] These two authors contributed equally to this work.

https://doi.org/10.1016/j.desal.2026.120111
Received 17 November 2025; Received in revised form 12 March 2026; Accepted 23 March 2026

through passive cooling, representing a significant loss of the captured solar resource; yet this temperature range aligns well with the thermal requirements of evaporation-based desalination processes [10]. Recovering this waste heat for simultaneous freshwater production would enable cogeneration systems that generate both electricity and freshwater from the same solar input, without requiring additional costly energy collection infrastructure [11,12]. This approach effectively converts a performance-limiting factor (panel heating) into a productive output.

Photovoltaic–thermal (PV/T) desalination systems have emerged to exploit this waste heat recovery opportunity. Early PV/T desalination configurations coupled PV panels with conventional solar stills, where the PV backsheet serves as the absorber surface for water evaporation [13]. Subsequent studies demonstrated performance improvements through structural modifications; for example, Badran et al. [14, 15] showed that integrating flat-plate collectors with solar stills increased water production by enhancing heat delivery to the evaporation surface. More recent implementations have incorporated active cooling systems with external heat exchangers to extract PV waste heat [16,17], achieving improved thermal management and water yields. Beyond conventional architectures, researchers have explored novel coupling approaches: PV–hydrogel systems use hygroscopic materials to simultaneously cool panels and harvest atmospheric water [18, 19], PV–multistage membrane distillation systems employ cascaded evaporation–condensation stages [20,21], and PV–thermoelectric hybrid systems convert thermal gradients into additional electrical output alongside desalination [22]. These diverse approaches highlight the versatility of PV/T integration, with a collective focus on material exploration and system configuration. However, they still lack comprehensive attention to critical engineering aspects, including system adaptability for large-scale deployment and real-world operational performance.

Despite these advances, current PV/T desalination systems face critical limitations that hinder deployment in decentralized settings. Most configurations rely on external components such as dedicated cooling pipes [16], separate condensation chambers [17], and auxiliary pumps to circulate working fluids between the PV panel and the desalination unit. This distributed architecture increases system complexity, installation costs, and spatial footprint. External piping also introduces thermal losses during heat transfer and creates additional potential failure points that require maintenance. For resource-constrained or remote applications where technical expertise and replacement parts may be limited, such complexity presents significant barriers to adoption. Furthermore, the separation between heat generation (PV panel) and water production (external still) necessitates careful fluid management and sealing, complicating system operation. These challenges underscore the need for more integrated designs that eliminate external components while maintaining cogeneration functionality.

Interfacial evaporation offers a pathway to more compact PV/T desalination systems. Unlike bulk heating approaches that warm the entire water volume, interfacial evaporation concentrates thermal energy at the liquid–vapor interface using porous wicking materials [23]. This localized heating minimizes conduction losses to the bulk water and enables direct integration with the PV backsheet without external heat exchangers. When coupled with PV panels, this enables a single-stage architecture in which the PV backsheet directly heats the evaporation wick. Recent implementations have explored various PV–interfacial evaporation coupling strategies [18–21], demonstrating the potential for improved energy utilization. However, these systems present certain challenges: some designs lack effective vapor–liquid separation, leading to salt accumulation on evaporation surfaces, while others achieve separation through external condensation chambers, reintroducing the complexity issues described previously. An integrated design that combines interfacial evaporation with in-situ membrane-based vapor separation could address both compactness and operational reliability.

A critical geometric parameter that affects PV/T desalination performance remains largely unexplored: the device inclination angle. For conventional PV systems, inclination angle optimization focuses solely on maximizing solar irradiance capture to enhance electrical output. For PV/T desalination systems, however, the inclination angle plays a dual role. It determines both the incident solar radiation (affecting electricity generation and thermal energy availability) and the gravity-driven flow dynamics through the evaporation wick (affecting water residence time, evaporation efficiency, and salt management). Steeper angles may improve solar capture but accelerate water flow, potentially reducing evaporation effectiveness. Shallower angles may extend water residence time but sacrifice radiation reception and risk salt accumulation due to insufficient drainage. Despite this critical trade-off, systematic investigations of inclination angle effects on cogeneration performance are rarely addressed in the PV/T desalination literature. Existing studies report performance at fixed angles chosen to match local latitude or maximize PV output, without examining how angle variations affect coupled system behavior. This knowledge gap prevents the optimization of PV/T desalination systems for real-world deployment scenarios.

This work addresses these gaps through three primary contributions. First, a compact PV/T interfacial evaporation membrane desalination system is developed that integrates capillary-driven evaporation and membrane distillation directly into the PV panel assembly, thereby eliminating external condensers and cooling pipes. The system uses commercially available materials (cotton fabric wicking, SiO_2-nanocoated aluminum condenser) to achieve 90% condensate collection efficiency with demonstrated durability over 5+ wet-dry cycles. Second, the first systematic investigation of the effects of inclination angle on PV/T desalination performance is conducted. Through controlled indoor experiments at three representative angles (5°, 15°, and 25°) under variable irradiance (400–1000 W/m^2), we characterize how tilt affects the coupled trade-offs between water flow dynamics, evaporation efficiency, and PV thermal management. Third, system performance and angle optimization strategies are validated through outdoor testing in both fixed-orientation and sun-tracking modes, demonstrating a 5% improvement in GOR and a 53.8% daily freshwater productivity with tracking. The resulting system provides a practical, scalable solution for distributed solar desalination in water-scarce regions, with design principles applicable to broader PV/T system development.

The remainder of this paper is organized as follows. Section 2 presents the system design and component development, including the operating principle, evaporator material selection and optimization, and condenser surface treatment and water collection channel design. Section 3 outlines the methodology employed to evaluate the performance of the device. This includes controlled indoor experiments to investigate the effects of inclination angle on coupled thermal, hydraulic, and electrical behavior, corresponding numerical simulations, and outdoor experiments conducted under fixed-orientation and sun-tracking operational modes. Section 4 presents the operational results, and Section 5 concludes with key findings and implications for the design of distributed solar desalination systems.

2. System design and optimization

2.1. Operating principle and structural design

The operating schematic and detailed structure of the compact PV/T interfacial evaporation device are shown in Fig. 1. The device consists of four main components: a photovoltaic panel integrated with a transparent enclosure (greenhouse), a hydrophilic wick for saltwater transport and evaporation, a distillation membrane, and a built-in condenser. The PV panel functions as a solar absorber, converting solar energy into electricity and heat. The transparent enclosure acts as a greenhouse, reducing convective and radiative heat loss from the absorber (i.e., the PV panel) to the surrounding environment while

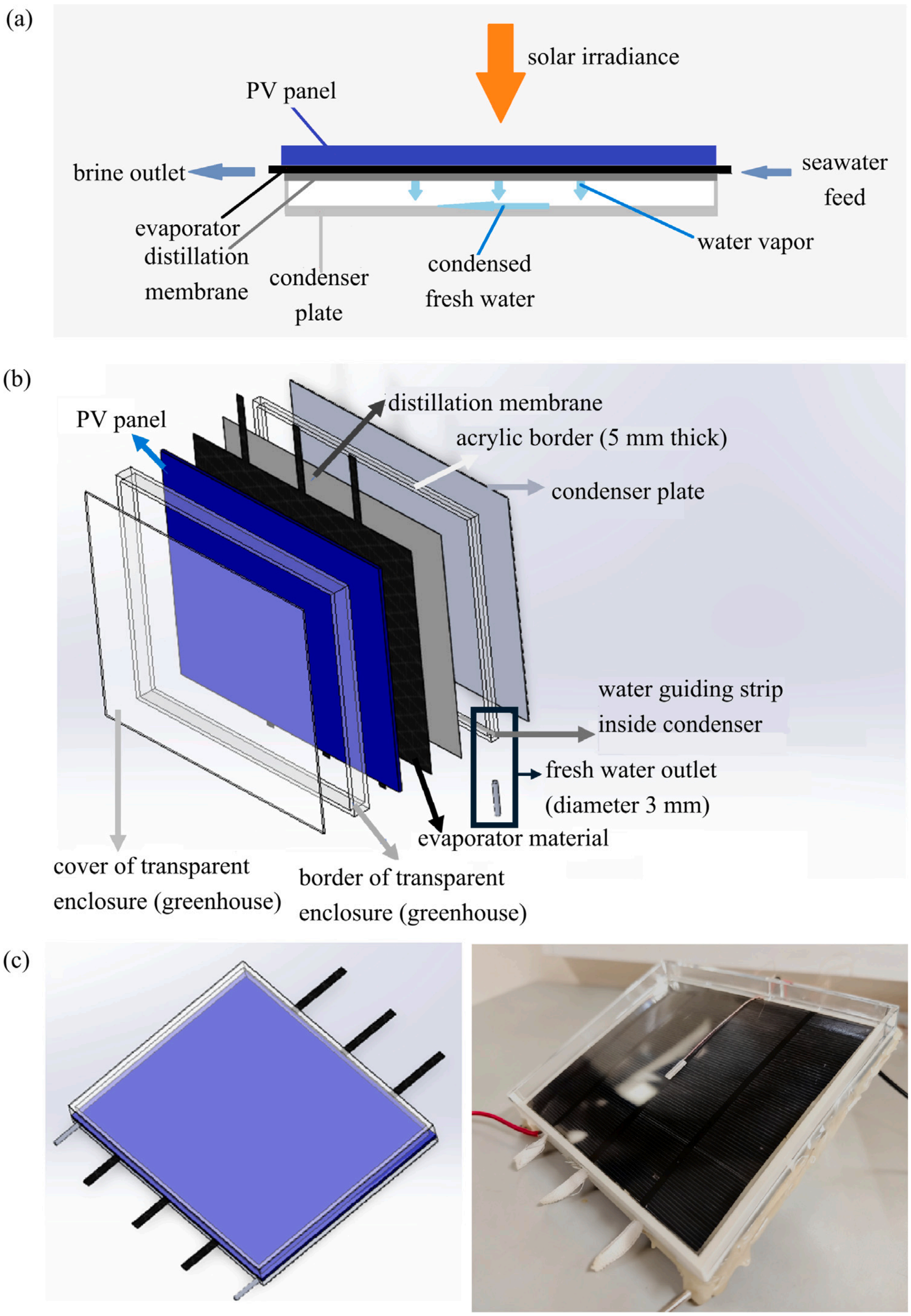

Fig. 1. A compact PV/T desalination device. (a) Operating principle showing the complete system with saltwater fed via capillary action through a hydrophilic wick attached to the PV backsheet. (b) Layered structure of the device: transparent acrylic enclosure (10 mm thick), commercial PV panel (5 mm thick), cotton evaporator surface, distillation membrane, SiO_2-nanocoated condenser plate, sea–island fiber water guiding strip, and freshwater outlet (3 mm diameter). (c) PV/T device after assembly (left: SolidWorks design; right: fabricated device).

having a minimal impact on power generation. A porous hydrophilic wick attached to the PV backsheet draws saltwater into the device through capillary action and gravity, acting as an evaporation surface that facilitates interfacial heating. A distillation membrane covers the interfacial evaporation material, enabling one-way transport of water vapor to the condenser while preventing the passage of liquid water and dissolved salts. The water vapor then condenses on the condenser plate, releasing heat to the surroundings, and the collected freshwater exits through the outlet ports of the condenser for retrieval. Table 1 presents the size parameters of each component of the experimental device. For all experiments, saltwater was prepared by dissolving sodium chloride (NaCl) in deionized water to achieve a salinity of 35,000 ppm (3.5 wt%), consistent with standard ocean salinity.

2.2. Design of the saltwater transport and evaporation component

As a critical component of the PV/T desalination device, the evaporator is designed to transport saltwater to the PV backsheet, absorb heat, and facilitate evaporation. To achieve optimized performance, two novel design features are introduced in this section.

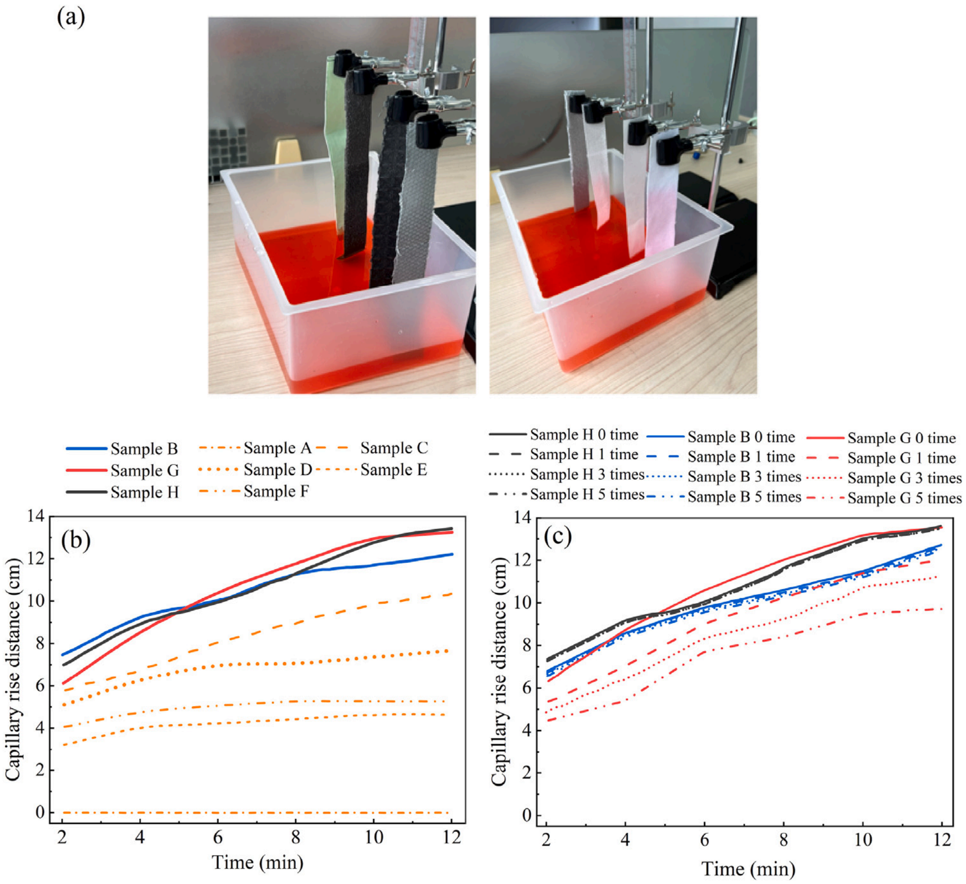

Fig. 2. Water transport testing of candidate evaporator materials. (a) Experimental setup: fabric samples (3 × 19 × 0.05 cm) suspended vertically with lower edges submerged in dyed water to visualize capillary rise over time. (b) Capillary rise distance as a function of time for all tested materials. (c) Durability testing through repeated wet-dry cycles (10-minute immersion followed by 20 min of drying at 70°C), conducted after 1, 3, and 5 cycles.

Table 1
Dimensions of each component of the fabricated PV/T desalination device.

Components	Surface area/Diameter	Thickness/Length
Transparent enclosure	13.5 cm × 16.5 cm	10 mm
PV panel	13.5 cm × 16.5 cm	3 mm
Evaporator material	13.5 cm × 16.5 cm	0.4 mm
Distillation membrane	13.5 cm × 16.5 cm	0.1 mm
Condenser plate	13.5 cm × 16.5 cm	2 mm
Acrylic border	2 mm × 16.1 cm (2 pieces), 2 mm × 13.5 cm (2 pieces)	5 mm
Freshwater outlet	Diameter: 3 mm	Length: 2 cm

2.2.1. *Selection of the evaporator materials*

The device relies on efficient and durable hydrophilic evaporator materials to transport saltwater and facilitate evaporation. In this study, we evaluated eight commercially available and cost-effective fabric materials, as presented in Table 2, to assess their performance and durability in saltwater transport.

To evaluate the water transport performance, a standardized capillary rise test was conducted. Fabric samples of uniform size (3 × 19 × 0.05 cm) were suspended vertically with their lower edges submerged in dyed water (Fig. 2a) and the rise distance was measured over time (Fig. 2b). Among the tested samples, Sample B (sea–island fiber), Sample G (pure sulfur cotton), and Sample H (cotton fiber) demonstrated the greatest capillary transport distances, exceeding 12 cm within 12 min. In contrast, all other materials exhibited a capillary rise of less than 8 cm.

The three best-performing materials were subsequently tested for durability through repeated wet-dry cycles (Fig. 2c), as actual operation requires sustained performance under repeated wetting and drying. Each cycle consisted of 10 min of water immersion followed by 20 min of drying at 70°C, with water transport tests conducted after 1, 3, and 5 cycles. Sample G (pure sulfur cotton) exhibited progressive degradation, with the capillary rise decreasing by approximately 30% after 5 cycles (the difference in value between the red solid line and the red dash–dot–dot line at 12 min in Fig. 2c). In contrast, Sample B (sea–island fiber) and Sample H (cotton fiber) maintained stable water transport performance throughout, showing no significant decline in functionality.

Based on these results, Sample H (cotton fiber) was selected as the evaporator material due to its high water transport rate, excellent durability under repeated cycling, and low cost. Scanning electron microscopy (SEM) analysis revealed the microstructure responsible for this performance (Fig. 3): the cotton fibers form an interconnected porous network with numerous microscale channels that facilitate efficient capillary water transport. This structure provides a microscopic explanation for the outstanding capillary water-transport properties of the material.

2.2.2. *Design of the saltwater transport strip configurations*

The saltwater transport strips deliver saltwater from the reservoir to the evaporator. Strip geometry significantly influences both water distribution uniformity and heat loss through the device walls. To optimize the design, six configurations varying in strip number (1–4) and placement (center vs. edge positions) were tested and compared, as shown in Fig. 4. The goal was to identify a configuration that balances efficient water delivery, minimal thermal losses, and reduced sealing complexity. All strips were designed with a uniform width of 5 mm to isolate the effects of number and placement.

Table 2
Candidate evaporator fabric materials with varying fiber compositions evaluated for water transport performance and durability. All samples were standardized to 3 × 19 × 0.05 cm for comparative testing.

Name	Fiber composition	Manufacturer
Sample A	Foam cotton	Yiwu Jieni E-commerce Co., LTD
Sample B	Sea–island fiber (Polypropylene fiber)	Guangzhou Youran Home Co., LTD
Sample C	Bamboo fiber	FumaiI Environmental Protection Technology Co., LTD
Sample D	Polyester fiber	Yiwu Youhui E-commerce Co., LTD
Sample E	88% Polyester fiber + 12% Nylon fiber	Yiwu Bingyang Network Technology Co., LTD
Sample F	Non-woven fabrics (Polyester)	Dongguan Xinran Daily Chemical Co., LTD
Sample G	Pure sulfur cotton	Guangzhou Yiyi Chemical Reagent Co., LTD
Sample H	Cotton fiber	Yongsheng Cotton Weaving Factory

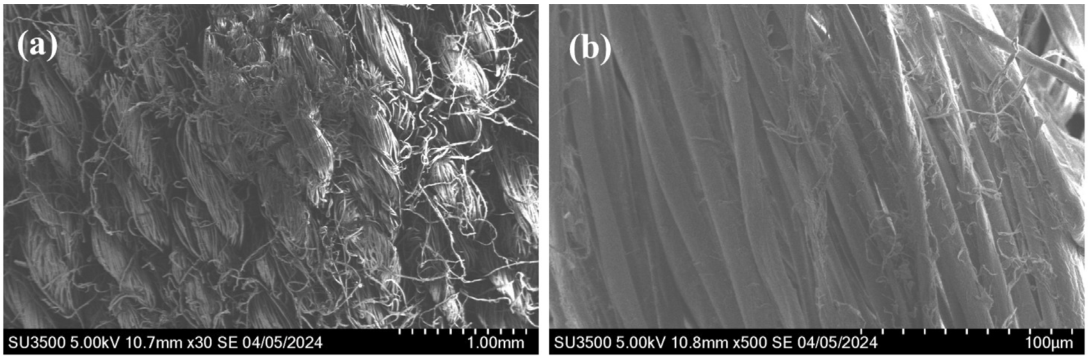

Fig. 3. Scanning electron microscopy (SEM) images of the selected cotton fabric at two magnifications: (a) 1 mm and (b) 100 μm. The interwoven fiber structure creates a three-dimensional porous network with interconnected micropores that facilitate efficient capillary water transport.

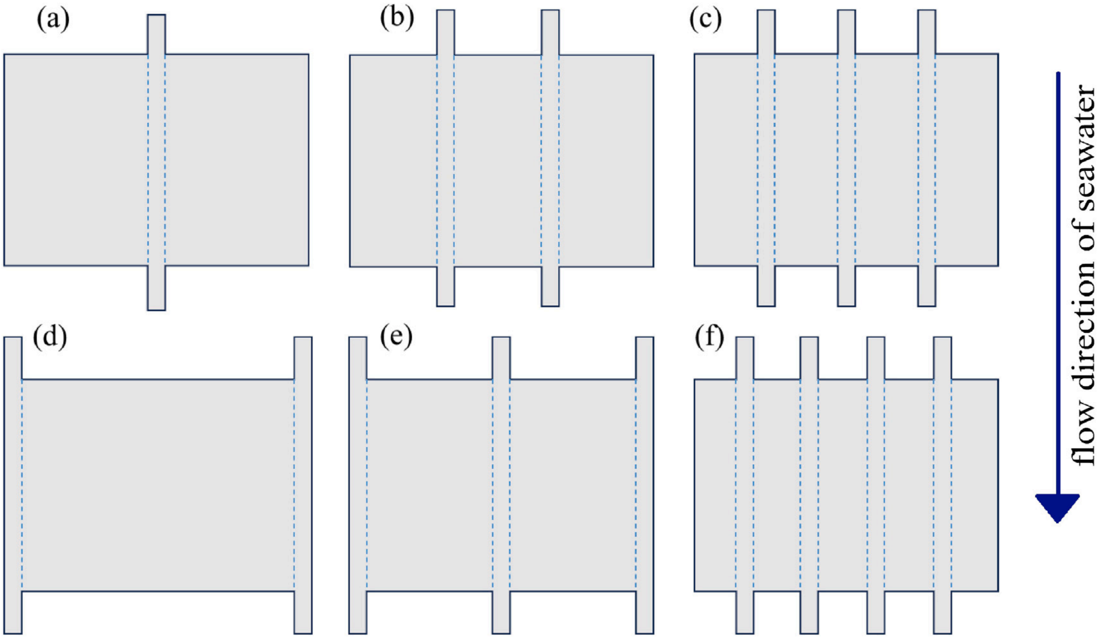

Fig. 4. Six saltwater transport strip configurations (all 5 mm wide) tested for water distribution performance: (a) single center strip, (b) two center strips, (c) three evenly distributed strips, (d) two edge strips, (e) two edge strips with one center strip, and (f) four evenly-distributed strips.

Cotton fabric samples with different strip configurations were mounted on aluminum plates to simulate actual operating conditions. The upper diversion strips were immersed in dyed water while the lateral diffusion pattern and wetting time were monitored. Strip number and placement significantly affected wetting speed and uniformity. The single and double strip designs (samples a, b, and d) produced slow and non-uniform wetting. Both the three evenly-distributed strips (samples c and e) and four strips (sample f) achieved rapid, uniform wetting with similar performance. However, the edge-positioned strips (sample e) caused excessive lateral water diffusion toward the device perimeter (Fig. 5), increasing the leakage risk at the sealing boundaries.

To further verify that the flow rate of sample c conforms to Darcy's law under steady-state conditions, flow rate tests were conducted for 15 min at three tilt angles (5°, 15°, and 25°) at a room temperature of 22°C, using the setup shown in Fig. 5d. The test results are shown in Fig. 5c. The measured flow rate ratios between angles closely match the ratios of their corresponding sine functions, confirming that flow through sample c follows Darcy's law under steady-state conditions. Based on these results, the three evenly-distributed strip configuration

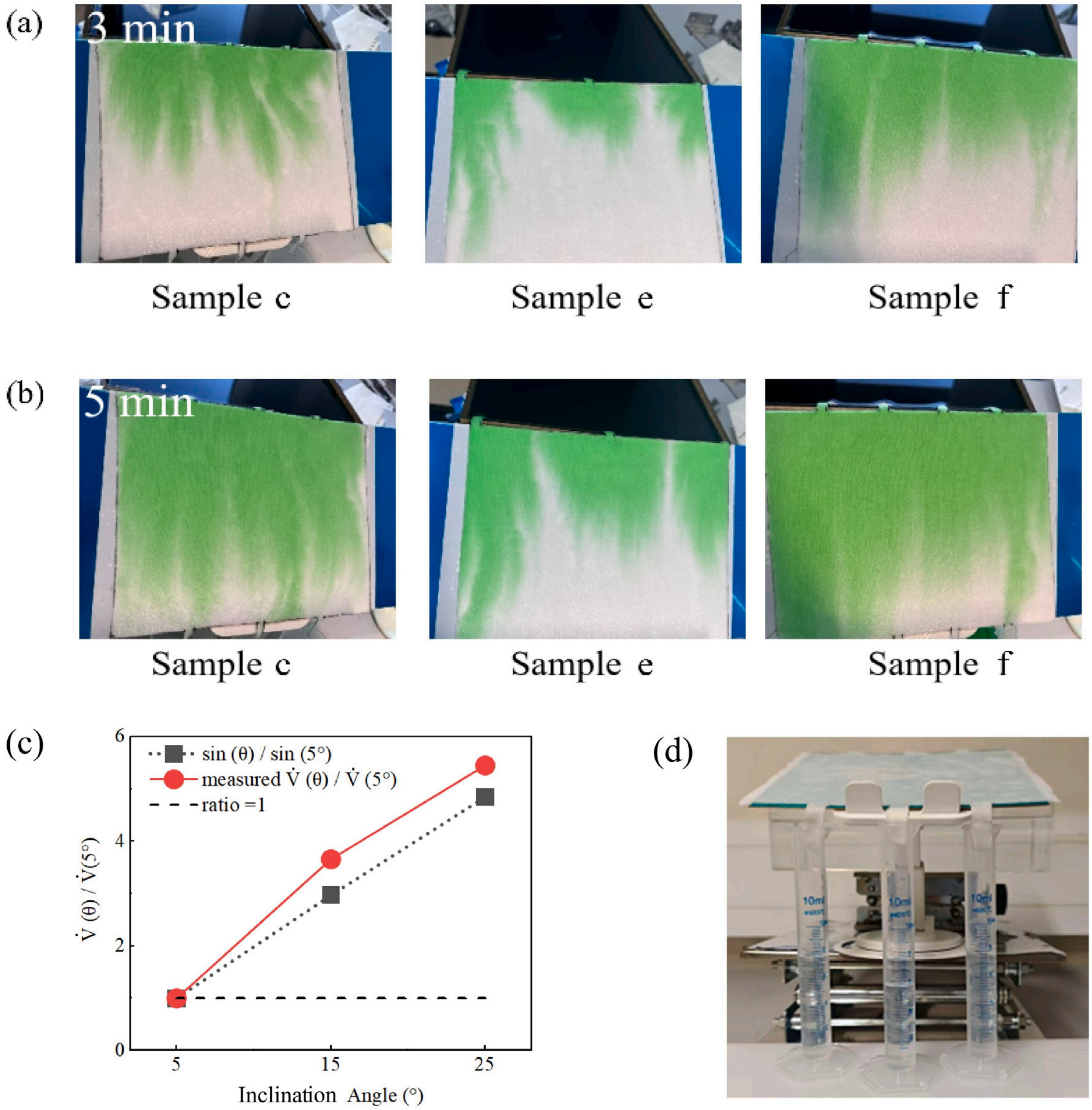

Fig. 5. Water distribution performance of saltwater transport strip configurations. Lateral wetting patterns of three evenly distributed strips (samples c and e) and four strips (sample f) after (a) 3 min and (b) 5 min contact with dyed water. (c) Steady-state flow rate test over 15 min confirming that sample c conforms to Darcy's law at different inclination angles (5°, 15°, and 25°). (d) Experiment setup for flow rate testing.

(sample c) was selected, as it provides efficient and uniform water distribution while minimizing structural complexity, heat loss pathways, and edge sealing risk.

2.3. Design of the condensation and freshwater collection component

Water vapor generated at the evaporation surface passes through the distillation membrane and contacts the condenser plate, where it condenses by releasing heat to the surroundings, and freshwater is collected. Effective heat dissipation requires the condenser plate to have high thermal conductivity, for which an aluminum plate with low thermal resistance was selected. During condensation, fine water droplets form on the surface of the condenser plate due to surface tension and adhere to it, necessitating specific design features to ensure efficient freshwater collection. Two such features are described in this section.

2.3.1. Selection of hydrophobic coatings for the condenser plate

The surface hydrophobicity of the condenser plate governs how efficiently water droplets roll off for collection. Surface wettability is quantified by the contact angle θ, defined as the angle between the tangent to the droplet and the solid surface at three-phase equilibrium (Fig. 6a). Contact angles $\theta > 90°$ indicate hydrophobic surfaces where droplets maintain near-spherical shapes and roll off readily, while $\theta < 90°$ indicate hydrophilic surfaces where droplets spread into films that adhere to the surface, reducing collection efficiency.

To enhance freshwater collection efficiency, three condenser plate surface conditions were compared: untreated aluminum (control), polytetrafluoroethylene (PTFE)-coated aluminum, and silicon dioxide (SiO_2)-nanocoated aluminum, all cut to 30 mm × 30 mm. Both coatings were applied via uniform spray coating to a thickness of approximately 5 μm. Contact angles were measured using an OCA Pro15 contact angle meter with the pendant drop method, averaging five measurements per sample to account for local surface variations.

The untreated aluminum plate exhibited hydrophilic behavior, with a contact angle of 74.5° ± 2.1° (Fig. 6b), causing droplets to spread completely across the surface and limiting collection efficiency. The PTFE coating improved hydrophobicity, increasing the contact angle to 98.2° ± 1.8° (Fig. 6c); however, the PTFE coating was prone to

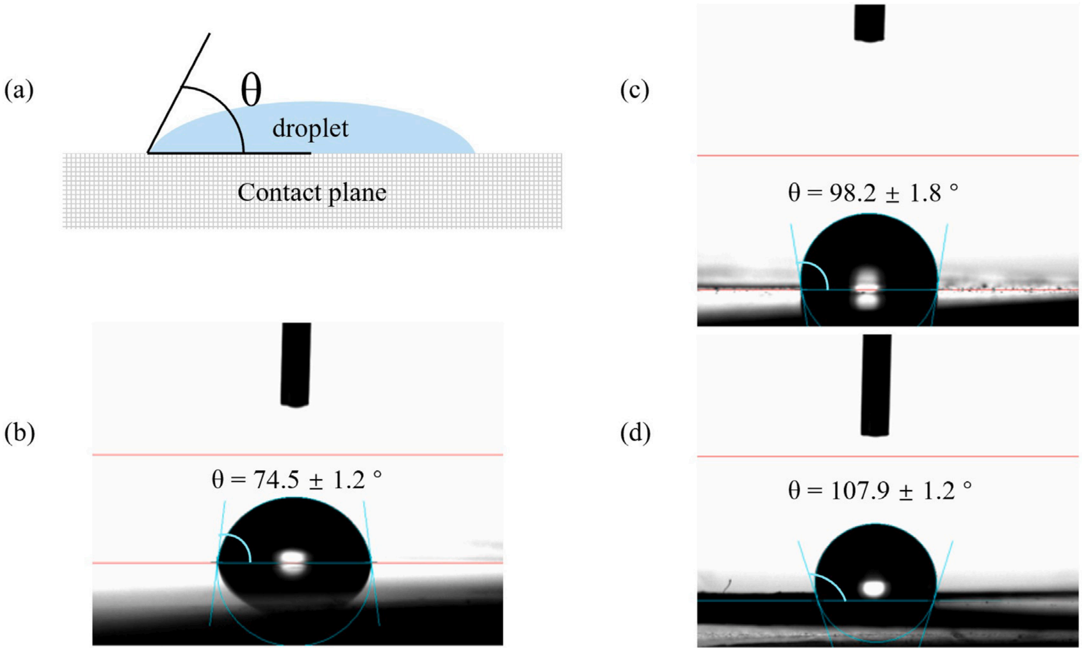

Fig. 6. Contact angle measurements for condenser plate surfaces with different coatings. (a) Definition of contact angle θ: angles ($\theta > 90°$) indicate hydrophobic surfaces that promote droplet roll-off. (b) Untreated aluminum: $\theta = 74.5° \pm 2.1°$ (hydrophilic; droplet spreads into film). (c) Teflon/PTFE-coated aluminum: $\theta = 98.2° \pm 1.8°$ (weakly hydrophobic; hemispherical droplet). (d) SiO_2-nanocoated aluminum: $\theta = 107.9° \pm 1.2°$ (strongly hydrophobic; near-spherical droplet with rolling angle $< 10°$). All measurements performed using an OCA Pro15 contact angle meter with five measurement points per sample.

micro-cracking during handling, resulting in measurement variability. The SiO_2 nanocoating achieved the highest hydrophobicity, with a contact angle of 107.9° ± 1.2° (Fig. 6d), where the nanoscale surface roughness creates a Cassie-Baxter state in which droplets remain nearly spherical with a rolling angle below 10°. Based on these results, SiO_2 nanocoating was selected for the condenser surface due to its superior hydrophobicity and mechanical stability.

2.3.2. Design of the water collection channels and outlets

To enhance freshwater collection efficiency, a 5 mm-high acrylic frame was designed to separate the condenser plate from the distillation membrane while forming a drainage channel. Sea–island fiber strips embedded within the frame utilize capillary action to guide droplets toward the outlets, preventing water accumulation along the edges (Fig. 7a). This material was selected due to its unique microstructure (Fig. 7b), which provides excellent water absorption and durability while facilitating the efficient removal of condensate that would otherwise be difficult to collect.

The positioning and number of outlet holes on the acrylic frame were also systematically optimized. Four outlet configurations were evaluated: a single center outlet (A), a single bottom-edge outlet (B), a single outlet at one-quarter width (C), and two symmetric bottom-edge outlets (D), as shown in Fig. 7c. To simulate operational conditions, water collection tests were conducted using water at 65°C with samples inclined at 10°. Two injection scenarios were tested for each configuration (Fig. 7d): injecting 1 mL of hot water at equal heights at both ends of the condenser plate and injecting 1 mL of hot water at one-quarter and three-quarters of the plate width. The collected water volume was recorded from the start of injection to 3 min post-injection.

The short term testing results demonstrated that the dual-outlet configuration (D) achieved a condensate collection efficiency, as defined in Eq. (1), of 70% (1.4 mL/2.0 mL), representing a 40% improvement over single-outlet designs (Fig. 7e). Furthermore, the symmetric dual-outlet arrangement ensured uniform drainage even when one outlet became partially obstructed, effectively mitigating the risk of complete clogging. However, the 3-minute tests resulted in temporary water retention on the fiber guides and condenser surface, without reaching the outlets, instead of permanent water loss. In the 20-minute tests, a significant portion of this retained water eventually drains, increasing the effective collection efficiency to approximately 90% to 95%. The remaining 5%–10% loss is attributed to water vapor diffusing out of the device through the seals.

$$\text{Condensate collection efficiency} = \frac{\text{Mass of collected freshwater}}{\text{Mass of evaporated brine}} \tag{1}$$

In summary, the optimized freshwater collection module incorporates three key design elements: a SiO_2-nanocoated condensation plate (contact angle: 107.9°, representing a 300% improvement in droplet mobility), sea–island fiber drainage guides (capillary transport rate: 0.8 mL/s), and dual symmetric bottom outlets (achieving a 90% condensate collection efficiency). Together, these integrated components enable efficient freshwater recovery from the condenser.

3. Performance evaluation methodology

Both indoor and outdoor experiments, along with numerical simulations, were conducted to evaluate the performance of the developed PV/T desalination device. Indoor experiments and numerical modeling investigated the effects of the inclination angle on system performance, an aspect rarely addressed in the literature, while outdoor experiments evaluated the effectiveness of a sun-tracking scheme for enhancing operational efficiency.

3.1. Performance assessment metrics

Several assessment metrics were used to evaluate device performance, as listed in Table 3 along with their measurement methods. The instrumentation and associated measurement uncertainties are summarized in Table 4. Detailed information on the indoor and outdoor experimental setups, including instrument placements, is shown in Fig. 8.

GOR is defined as:

$$\mathrm{GOR} = \frac{M_e h_{fg} + W_{pv}}{A \cdot S}, \tag{2}$$

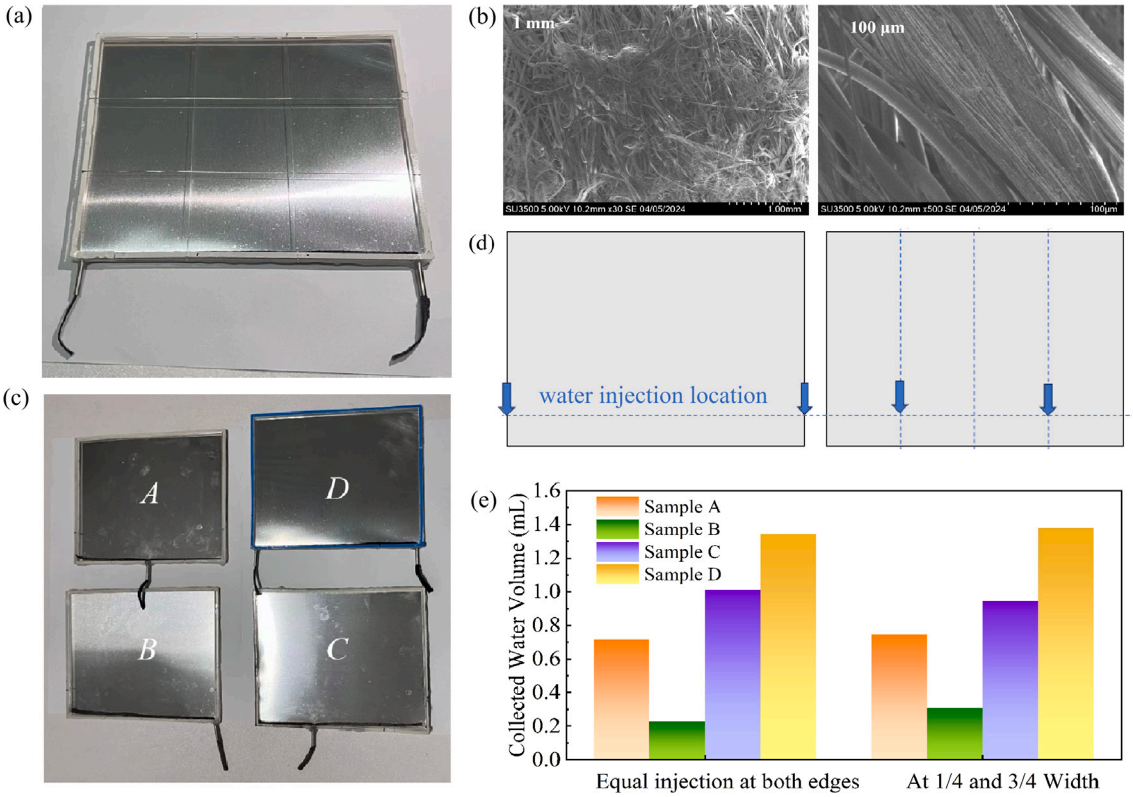

Fig. 7. Optimization of the condensation component. (a) Complete condenser assembly showing a 5 mm-high acrylic frame forming flow channels, with embedded sea–island fiber strips (capillary water conduction rate: 0.8 mL/s) guiding droplets toward outlet holes. (b) SEM images of sea–island fiber at two magnifications (left: 1 mm; right: 100 μm). (c) Four outlet configurations evaluated: (A) single center outlet, (B) single bottom-edge outlet, (C) single outlet at one-quarter width, and (D) two symmetric bottom-edge outlets. (d) Hot water injection testing under two scenarios with different injection locations: equal injections at both edges (left); injection at one-quarter and three-quarters width (right). (e) Collected water volume for each configuration under both injection scenarios.

Table 3
Performance assessment metrics and measurement methods.

Assessment metrics	Definition	Measurement method
Gain-output ratio (GOR)	The overall efficiency of converting solar irradiance into evaporation enthalpy and electrical power	Solar irradiance - radiometer Mass of evaporated water - electronic balance Power generation - multimeter
Freshwater yield (productivity) [kg/m^2 h]	Collected freshwater amount per unit area per unit time	Mass of collected freshwater - electronic balance
Power generation efficiency	PV panel power generation as a percentage of incident solar flux	Power generation - multimeter Solar irradiance - radiometer
Irradiance enhancement factor	Ratio of daily accumulated Plane-of-Array (POA) irradiance to daily accumulated Global Horizontal Irradiance (GHI)	Solar irradiance - radiometer

Table 4
Instrumentation used in indoor and outdoor experiments, including measured variables and measurement uncertainties.

Name	Measured variable	Manufacturer	Measurement uncertainties
Radiometer	Incident solar irradiance	Jinzhou Sunshine Meteorological Co., Ltd.	± 5%
Thermocouples	Temperatures of PV backsheet, evaporator and condenser plate	Suzhou Teans Electronic Industry Co., Ltd.	± 0.2% + 0.7°C
Multimeter	PV electrical output	Bolin Electronics Co., Ltd.	± 0.5%
Electronic balance	Mass of water	Dongguan Changxie Electronics	± 0.3 g

where M_e [kg/h] is the total mass of evaporated water, h_{fg} [kJ/kg] is the latent heat of vaporization, W_{pv} [W] is the electrical power output from the PV panel, A [m^2] is the surface area of the device, and S [W/m^2] is the incident solar irradiance. Furthermore, daily GOR for outdoor experiments is defined as:

$$\mathrm{GOR}_{\mathrm{daily}} = \frac{\int_{t_i}^{t_o}(M_e h_{fg} + W_{pv})\,dt}{A\int_{t_i}^{t_o} S\,dt}, \tag{3}$$

where t_i and t_o are the start and end times of the outdoor experiments, taken to be 10:00 and 17:00 in this work.

Freshwater yield is calculated as:

$$\text{Freshwater yield} = \frac{M_{t_0+\Delta t} - M_{t_0}}{\Delta t \cdot A}, \tag{4}$$

where $M_{t_0+\Delta t}$ [kg] is the mass of water collected at $t_0 + \Delta t$, M_{t_0} [kg] is the mass of water collected at t_0 and Δt [h] is the duration. For indoor experiments, t_0 is set to 20 min (after the transient phase) from the start

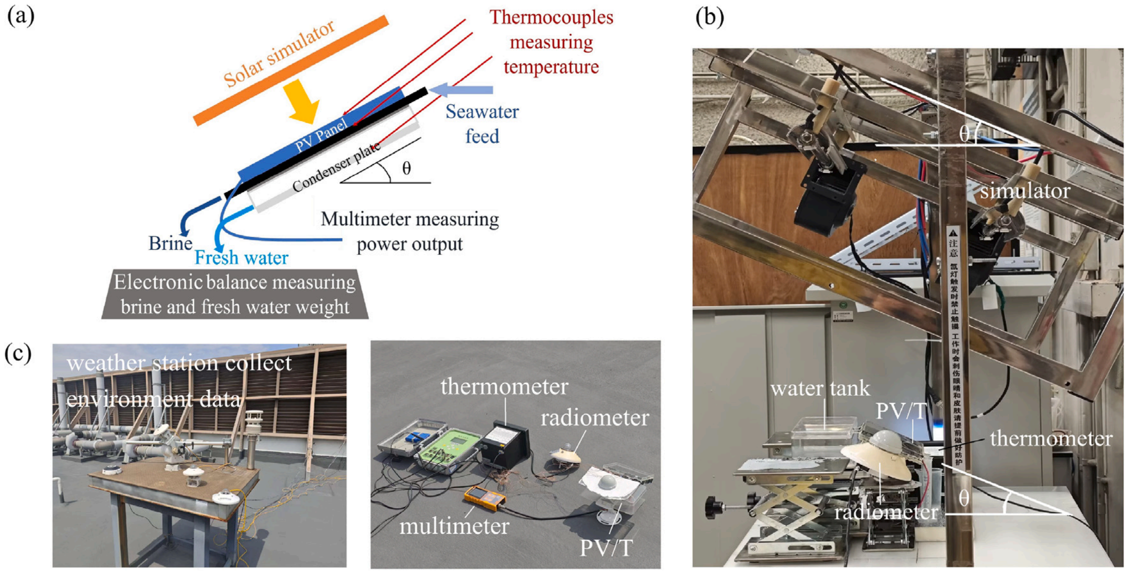

Fig. 8. Experimental setup. (a) Schematic diagram of the indoor experimental setup with the device inclined at 5°, 15°, or 25° under a solar simulator aligned parallel to the device surface. Measured variables include solar simulator irradiance (400–1000 W/m^2), PV panel power output (multimeter), temperatures at three locations along the evaporator and condenser surfaces (thermocouples), saltwater flow rate, and freshwater production rate (electronic balance, 0.01 g precision). (b) Photograph of the indoor experimental setup showing device orientation and sensor placements. (c) Outdoor experimental setup on the rooftop of the Hong Kong Polytechnic University, with the device oriented at 22° inclination on an unobstructed rooftop. Ambient conditions: 18–25°C air temperature, partly cloudy weather, and wind speed 0–6 m/s. Tests were conducted in both fixed-orientation and sun-tracking modes.

of the experiments to accurately reflect steady-state operation, and Δt is set to 60 min.

The irradiance enhancement factor (IEF) quantifies the increase in solar irradiance received by a tilted or sun-tracking device relative to a horizontal surface, defined as the ratio of daily accumulated plane-of-array (POA) irradiance to daily accumulated global horizontal irradiance (GHI):

$$\mathrm{IEF} = \frac{\int_{t_i}^{t_o} \mathrm{POA}\ dt}{\int_{t_i}^{t_o} \mathrm{GHI}\ dt} \tag{5}$$

3.2. Experimental method

The inclination angle is a critical parameter influencing PV/T device performance. For fixed PV modules, it directly affects incident solar irradiance, which in turn impacts both PV power output and evaporator surface temperature. Simultaneously, the inclination angle governs the gravity-driven flow of water through the evaporation wick, affecting flow velocity, residence time, and distribution uniformity. Steeper angles promote faster water flow, reducing the risk of salt accumulation but potentially decreasing evaporation efficiency due to reduced water residence time on the heated surface.

Indoor experiments were conducted at three representative inclination angles: 5° (near-horizontal), 15° (moderate angle), and 25° (steeper angle to explore performance limits). To maintain consistent irradiance across all angles, the solar simulator lamp was adjusted to remain parallel to the PV/T surface each time the inclination was changed. This intentional design choice isolates the effect of inclination on gravity-driven flow, allowing changes in flow behavior to be attributed to the gravitational component rather than variations in irradiance, which is strongly dependent on tilt angle.

Each test ran for 80 min, based on preliminary observations that the PV panel with the greenhouse enclosure reached thermal equilibrium within approximately 20 min and remained stable for the remaining 60 min. Temperature, power output, and other relevant parameters were recorded at 20-minute intervals during the stable phase. To maintain experimental consistency, a 40-minute cooling interval was introduced between consecutive tests. This cooling phase allowed the equipment to return to its initial temperature and minimized interference from residual freshwater left over from previous tests. Fig. 8a and b illustrate the experimental setup, including instrumentation for measuring temperature, irradiance, power output, and water production. During these tests, solar irradiance incident on the device was varied from 400 to 1000 W/m^2 to simulate a range of weather conditions from overcast to fully sunny, while all other ambient conditions were kept constant to isolate the inclination angle as the sole variable.

Performance evaluations at each angle and irradiance level were based on a single 80-minute steady-state experiment. However, key parameters such as temperature and power output were recorded at multiple time points during the steady-state phase (20 – 80 min), and average values were reported. Key results, such as freshwater productivity and brine flow rate, were derived from comprehensive measurements over this longer steady-state period, thus improving the reliability of each data point. All tilt angle experiments were repeated twice to verify trends, and the presented data (Fig. 11) demonstrate consistent regularity in the experimental results across the entire parameter range.

Outdoor experiments were conducted on an unobstructed roof at Hong Kong Polytechnic University in March 2026. In fixed-orientation mode, the device was installed at a fixed 22° inclination, which matches the optimal angle for PV installation in Hong Kong. In sun-tracking mode, the surface azimuth angle of the device was manually adjusted throughout the day to align with the solar azimuth angle, while the inclination angle was fixed at 22°. Tests were carried out under partly cloudy conditions, with ambient temperatures ranging from 18 to 25°C and wind speeds below 6 m/s. Fig. 8c shows the complete experimental setup with sensor placements, and Fig. 12 shows the detailed environmental information.

3.3. Numerical method

To cross validate the experimental results, COMSOL Multiphysics 6.2 was employed to simulate the coupled processes of fluid flow, heat transfer, and mass transfer within the device (Fig. 9a). The primary physical phenomena modeled include Darcy flow within the cotton evaporation wick, interfacial evaporation, water vapor transport toward the condenser, and subsequent condensation. To resolve the

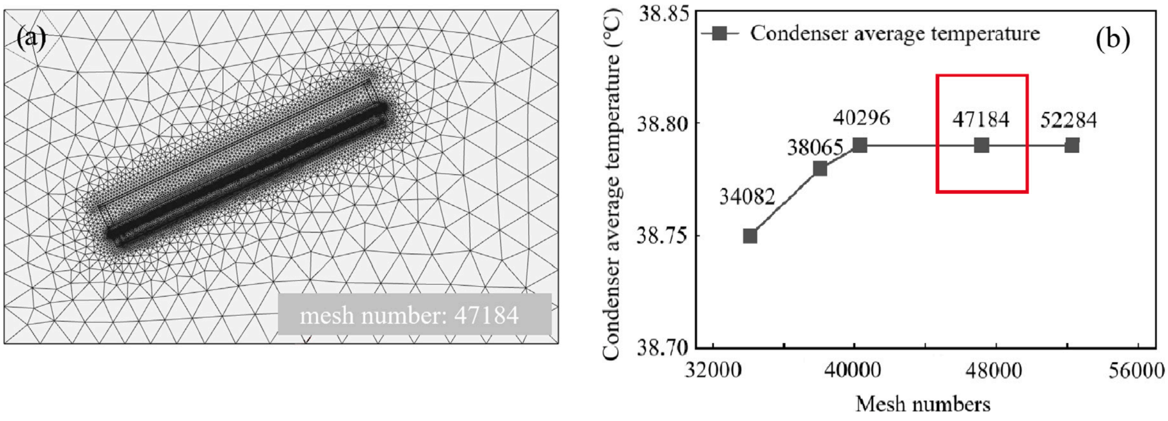

Fig. 9. Geometry and mesh of the simulation model: (a) Overall computational domain and mesh; (b) Mesh convergence test results for five different mesh densities, with the selected mesh of 47,184 elements indicated.

coupled heat transfer, moisture transport, and Darcy flow problem, the Heat Transfer in Moist Air and Moisture Transport in Air interfaces, as well as Darcy's Law modules, were implemented. Utilizing the dimensions of each component from the experimentally designed PV/T system (Table 1), a two-dimensional model was constructed. The 2D plane represents a cross-sectional view parallel to the direction of water flow.

3.3.1. Geometry and assumptions

The model encompasses the following domains: the acrylic cover, the PV panel, the cotton wick, the aluminum condenser, the air gap between the acrylic cover and the PV, the air space within the condenser, and the surrounding air of the PV/T device. Solar energy is applied as a heat flux incident on the PV surface, leading to its heating. This heating, in turn, raises the temperature of the air within the greenhouse and the water flow within the cotton wick. The heated water vapor subsequently evaporates from the lower surface of the cotton wick and eventually condenses onto the condenser plate. The following assumptions were made to ensure model accuracy while reducing computational complexity:

1. The simulation is in a steady-state.
2. Moisture transport through the PV panel is negligible; therefore, moisture transport in the air gap between the acrylic cover and the PV panel is neglected.
3. Condensation occurs exclusively on the condenser surface, defined as the boundary at which relative humidity (RH) reaches 1.
4. The PV panel domain is subjected to a constant surface heat flux equal to the absorbed solar energy minus the electrical power output.

3.3.2. Governing equations and boundary conditions

The energy conservation equations that govern the heat transfer processes for each domain are defined as follows:

For the solid domains:

$$\rho_s c_{p,s} \frac{\partial T_s}{\partial t} = \nabla \cdot \left(k_s \nabla T_s\right) + q_{\mathrm{gen}} \tag{6}$$

where ρ_s [kg/m^3], $c_{p,s}$ [J/kg], and k_s [W/(m K)] are the density, specific heat capacity, and thermal conductivity of the material; q_{gen} is the internal heat source.

For the air domain between the acrylic cover and PV panel:

$$\rho_a c_{p,a} \left(\frac{\partial T_a}{\partial t} + \mathbf{u} \cdot \nabla T_a\right) = \nabla \cdot \left(k_a \nabla T_a\right) \tag{7}$$

where $\rho_a, c_{p,a}, k_a$ are the density, specific heat capacity, and thermal conductivity of air; $\mathbf{u}$ [m/s] is the naturally induced air velocity, which can be solved using the Boussinesq approximation.

For the air domain within the condenser:

$$\rho_m c_{p,m} \left(\frac{\partial T_m}{\partial t} + \mathbf{u} \cdot \nabla T_m\right) = \nabla \cdot \left(k_m \nabla T_m\right) + \dot{m}_v h_{fg} \tag{8}$$

where $\rho_m, c_{p,m}, k_m$ are the density, specific heat capacity, and thermal conductivity of moist air; $\dot{m}_v$ [kg/m^3] is the local condensation/evaporation rate of water vapor, obtained from the mass transfer equation; h_{fg} [kJ/kg] is the latent heat of vaporization.

For the evaporator domain subjected to Darcy flow:

$$\left(\rho c_p\right)_{\mathrm{eff}} \frac{\partial T}{\partial t} + \left(\rho c_p\right)_f \mathbf{u}_D \cdot \nabla T = \nabla \cdot \left(k_{\mathrm{eff}} \nabla T\right) + q_{\mathrm{porous}} \tag{9}$$

where $\left(\rho c_p\right)_{\mathrm{eff}} = \phi \left(\rho c_p\right)_f + (1-\phi)\left(\rho c_p\right)_s$ [J/(m^3 K)] is the effective volumetric heat capacity of the porous medium, with ϕ [–] representing the porosity of the cotton wick; k_{eff} [W/(m K)] is the effective thermal conductivity; $\mathbf{u}_D = -\frac{K}{\mu}\nabla P$ [m/s] is the Darcy velocity, with K [m^2] the permeability of the wick and μ [Pa s] the dynamic viscosity of water; and q_{porous} [W/m^3] is the heat source within the porous medium.

The mass conservation equation governing the diffusive and convective mass transfer processes is:

$$\frac{\partial C_v}{\partial t} + \mathbf{u} \cdot \nabla C_v = \nabla \cdot \left(D_{va} \nabla C_v\right) + S_v \tag{10}$$

where C_v [kg/m^3] is the water vapor concentration; D_{va} [m^2/s] is the water vapor diffusion coefficient in air; S_v [kg/(m^3 s)] is the water vapor source term, which represents the steam generated or consumed by the phase change (evaporation or condensation). The water vapor condensation/evaporation rate $\dot{m}_v$ and the source term S_v satisfy $\dot{m}_v = S_v \cdot V$, where V [m^3] is the volume of the control volume.

Regarding the boundary conditions, all boundaries of the air domain surrounding the PV/T components are set to a temperature of 22°C and a relative humidity (RH) of 0.5. The convective heat transfer coefficient between air and surfaces for both the acrylic surface and the condenser plate surface is specified as 10 W/(m^2 K) [24]. The surface heat source of the PV is defined as $\alpha_{pv} S(1-\eta_{\mathrm{pv}})$. The wick permeability (K) is calculated from measured mass flow data collected under varying inclination angles in normal room light conditions (approximately 0 W/m^2).

3.3.3. Material properties

Thermophysical properties of air, aluminum, and water, including parameters such as density, thermal conductivity, specific heat capacity, and viscosity, were obtained from the COMSOL Multiphysics material library. The remaining material properties are summarized in Table 5.

3.3.4. Mesh convergence test

To ensure the accuracy of the simulation results, mesh convergence was assessed by monitoring the average condenser temperature under

Table 5
Material properties used in the numerical simulations.

Description	Symbols	Value	Data source
Diffusion coefficient of vapor in air	D_{va}	2.6×10^{-5} m^2/s	[25]
PV absorption ratio of solar irradiance	α_{pv}	0.8	Measurement
PV generation efficiency	η_{pv}	0.1	Measurement
Porosity of the cotton wick	ϕ	0.85	[26]
Equivalent permeability of water in cotton wick at 5°	K	3.179×10^{-11} m^2	Measurement
Equivalent permeability of water in cotton wick at 15°	K	2.618×10^{-11} m^2	Measurement
Equivalent permeability of water in cotton wick at 25°	K	1.998×10^{-11} m^2	Measurement
Thermal conductivity of cotton wick	k_c	0.05 W/(m K)	[26]
Heat capacity of cotton wick	C_{p_c}	1300 J/(kg K)	[26]
Density of cotton wick	ρ_c	400 kg/m^3	[26]
Thermal conductivity of acrylic	k_a	0.16 W/(m K)	[27]
Heat capacity of acrylic	C_{p_a}	1420 J/(kg K)	[27]
Density of acrylic	ρ_a	1190 kg/m^3	[27]
Thermal conductivity of PV panel	k_{pv}	0.2894 W/(m K)	[28]
Heat capacity of PV panel	$C_{p_{pv}}$	1552 J/(kg K)	[28]
Density of PV panel	ρ_{pv}	1190 kg/m^3	[28]

conditions corresponding to a device inclination angle of 25° and an irradiance of 400 W/m^2. As shown in Fig. 9b, the results confirm that the selected mesh size of 47,184 elements achieves stable convergence, with negligible variation upon further refinement; therefore, this mesh was adopted for all simulations.

4. Results and discussion

4.1. Effects of inclination angle in indoor conditions

The performance of the integrated PV/T system exhibits the following trends with increasing inclination angles: PV efficiency remains stable, the water mass flow rate increases, evaporator and condenser temperatures vary slightly, and freshwater productivity remains nearly constant. The detailed experimental and simulation results are discussed as follows.

The temperature and power output of the polycrystalline silicon photovoltaic (PV) panels under standard 1-sun irradiance are presented in Fig. 10a. During the initial warm-up phase, the power output decreases and subsequently stabilizes once the panel temperature exceeds approximately 50°C. As illustrated in Fig. 11a, the panel temperatures for all three inclination angles consistently remain above 50°C. This explains the negligible variation in PV electrical efficiency with respect to the inclination angle, as shown in Fig. 11f.

As shown in Fig. 10b, the brine mass flow rate increases with the inclination angle. A steeper inclination increases the absolute elevation difference between the inlet and outlet, raising the hydrostatic pressure gradient across the evaporator wick. This, in turn, enhances the Darcy velocity and the resulting mass flow rate of brine in the evaporator.

Regarding the temperature field, as shown in Fig. 11a and b, both the simulated and experimental results indicate that the temperature differences across the inclination angles of the evaporator wick and condenser remain minimal at all tested angles. The standard deviations of the temperatures do not exceed 0.6°C across all three angles (Fig. 11e), and the experimental results show slightly higher standard deviations than the simulated results. These small temperature differences between angles arise primarily because the total solar energy input to the system is identical for all inclination angles, and the Darcy flow velocity within the thin cotton wick is too low to induce significant convective heat removal. Consequently, the larger inclination angle, which is associated with a higher Darcy velocity, enhances heat removal via water flow only slightly, resulting in a minor reduction in both the evaporator wick and condenser temperatures.

Despite the differences in temperature and flow rate described above, freshwater productivity remains nearly constant across all three tested inclination angles in both experiments and simulations (Fig. 11d), yielding approximately 0.65 kg/m^2/h under 1000 W/m^2 irradiance. Provided that the porous evaporator wick does not dry out, the results demonstrate that the total evaporation rate from the evaporator is proportional to the absorbed heat flux (Fig. 11d), which is independent of the inclination angle in our experiments. Therefore, the evaporation rate, freshwater production rate, and GOR are effectively independent of the inclination angle, despite the differences in brine flow rate.

The 6–8°C temperature difference between the evaporator and condenser (Fig. 11c) drives efficient condensation, achieving a condensate collection efficiency of over 90% and ensuring that the measured freshwater productivity closely reflects the actual evaporation rate and GOR behavior. Additionally, a small amount of water vapor may escape the system through minor gaps at component interfaces before condensing.

In summary, both GOR and the PV electrical efficiency of the device (Fig. 11f) vary only slightly across the three tested inclination angles. We therefore conclude that the inclination angle has no significant effect on freshwater productivity, and the device should be oriented at the location-specific optimum angle for electricity generation in practice.

4.2. Outdoor operational performance

Outdoor experiments were conducted over two consecutive days in March 2026 under partly cloudy conditions: one day in the fixed-orientation mode and the other in sun-tracking mode. Detailed environmental data are presented in Fig. 12.

In the fixed-orientation mode, the device was operated continuously throughout the day at a 22° south-facing inclination. The temporal evolution of system temperatures and freshwater production is shown in Fig. 13. During peak POA irradiance periods (10:30–13:30, Fig. 12b), the evaporator surface temperature fluctuated between 51.7–58.4°C, while the condenser temperature ranged from 36.7–55.0°C, yielding a temperature difference of 3.2–15.0°C that drives efficient vapor condensation (Fig. 13b). The abrupt rise in condenser temperature observed during 11:00–12:00 is attributed to a concurrent reduction in wind speed (Fig. 12c), which decreased the convective heat transfer coefficient at the condenser surface and consequently reduced heat dissipation, causing the condenser temperature to rise temporarily.

Freshwater productivity followed variations in solar irradiance throughout the day. Daily freshwater production totaled 1.73 kg/m^2 over the 10:00–17:00 test period, with peak productivity of 0.412 kg/m^2/h recorded between 11:30–12:00 when the POA irradiance reached approximately 950 W/m^2. The peak GOR of 0.642 was achieved at the same interval (Fig. 13 a and Table 6).

In sun-tracking mode, the device was rotated along a vertical axis every 10 min to adjust its surface azimuth angle, aligning it with the solar azimuth angle throughout the day while maintaining a fixed inclination angle of 22°. Since the experiments for the two modes were conducted on different days, their weather conditions were similar

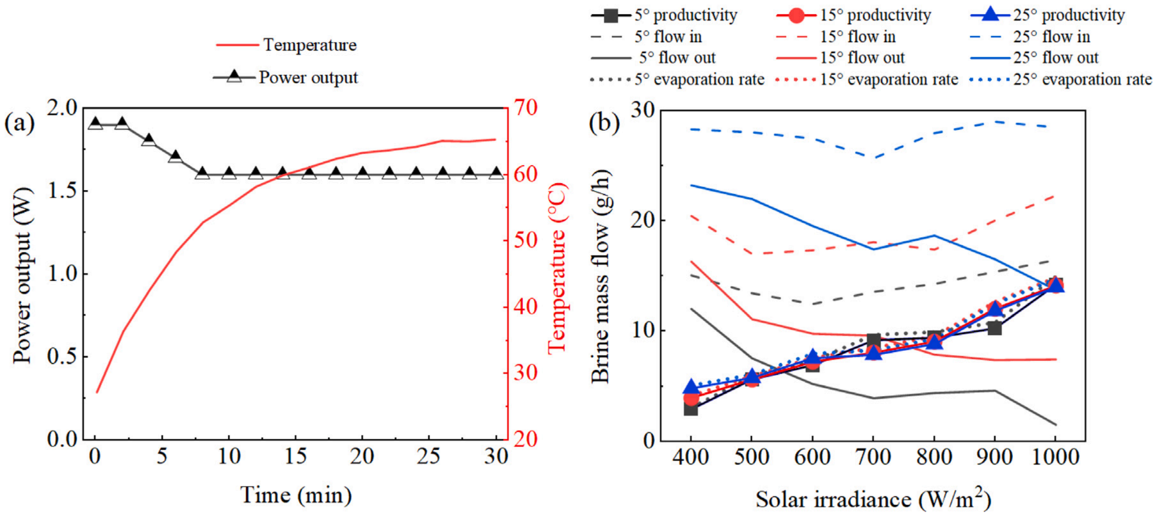

Fig. 10. (a) Power output and temperatures of the polycrystalline silicon PV panel used in the experiment over 30 min under 1 sun irradiance (left axis: power output [W]; right axis: temperature [°C]). (b) Brine mass flow rates at different inclination angles and irradiance levels during 1-hour steady-state tests. Dashed lines represent brine inlet mass flow, while solid lines represent brine outlet mass flow. The dotted lines represent the evaporation rate (brine inlet–outlet difference) and solid lines with markers represent freshwater productivity.

but not identical, leading to the differing GHI variations observed in Fig. 12b and e. Compared to the fixed-orientation mode, sun-tracking maintained evaporator temperatures above 55°C for over five hours, with a 15–20°C temperature difference between the evaporator and condenser (Fig. 13d), indicating more efficient condensation. This sustained thermal performance can be attributed to both the increased POA irradiance captured through azimuth tracking and the higher average wind speed during the tracking experiment, which enhanced the convective heat transfer coefficient at the condenser surface and resulted in lower condenser temperatures. Freshwater production increased correspondingly, with a peak productivity of 0.465 $kg/m^2/h$ (12.9% higher than the fixed-orientation mode) and a cumulative daily production of 2.66 kg/m^2 (53.8% higher than the fixed-orientation mode). This increased productivity is the result of a combined effect: (1) higher POA irradiance received through tracking, as demonstrated by an irradiance enhancement factor (IEF) of 1.26, a 23.5% increase compared to the fixed-orientation mode (IEF = 1.02); and (2) lower condenser temperatures reflected by an increase in the daily GOR (calculated using POA irradiance as the denominator) to 0.366, representing a 5% improvement over the fixed-orientation mode. A full performance comparison between the two modes is provided in Table 6.

Both operating modes exhibited a marked increase in GOR after 15:00, coinciding with declining irradiance, with peak GOR occurring at 17:00. This behavior is attributable to the thermal inertia of the greenhouse enclosure: the 10-mm acrylic cover, enclosed air gap, and thermal mass of the PV/T assembly together constitute a system of considerable thermal storage capacity. During periods of high irradiance, this structure absorbs and stores substantial thermal energy. As irradiance declines, the external heat input decreases, but the internally stored heat continues to be released to the evaporation wick in a delayed manner, sustaining evaporation and driving the continued rise in GOR even as solar input falls.

4.3. Long-term operational considerations and brine management

The long-term operational stability of the system was assessed by examining potential reliability pathways through inherent design features and straightforward maintenance considerations.

The gravity-driven flow design allows saline water to pass continuously through the evaporation layer, which may help mitigate salt accumulation at the evaporation interface. This was supported by the absence of visible salt crystallization on the evaporation fabric surface following the preliminary five-day operational test.

The distillation membrane physically separates water vapor from brine, inherently preventing direct contact between dissolved salts and the condensation surface and offering a potential means to alleviate scaling. During a preliminary five-day test involving multiple wet-dry cycles, no significant performance degradation of the system was observed. Visual inspection of the condenser surface after testing confirmed no salt deposits, consistent with effective vapor–liquid separation by the membrane.

The cotton fabric evaporation material demonstrated promising durability, maintaining stable water transport performance over more than five wet-dry cycles (Fig. 2c). The distillation membrane and SiO_2 nanocoating similarly showed no visible degradation following repeated wet-dry cycling, suggesting that all primary components are compatible with the proposed maintenance protocol. To support long-term operation, flushing the system with freshwater every 7–10 days is considered a feasible maintenance pathway to remove accumulated salts from the evaporation fabric and prevent crystallization.

Comprehensive durability testing over months or years of continuous operation remains essential to fully validate long-term reliability and constitutes a primary focus for future work, alongside further optimization of system design and maintenance strategies. In particular, systematic characterization of produced water quality and salt rejection performance over extended operation will be essential to fully establish the system's suitability for practical deployment.

5. Conclusions

A compact PV/T desalination device that simultaneously generates electricity and produces freshwater from a single photovoltaic panel has been developed. Waste heat from the PV backsheet drives interfacial evaporation, with water vapor being separated from brine by a distillation membrane and condensed on an integrated condenser.

Systematic component optimization was essential to device performance. Cotton fabric was selected as the evaporator material for its high capillary water absorption rate (0.8 mL/s) and durability, maintaining stable water transport over more than five wet-dry cycles. Its interwoven porous fiber network provides numerous microscale channels that facilitate efficient capillary water transport, while the three-strip configuration ensures uniform water distribution across the evaporation surface. For the condenser, SiO_2 nanocoating on aluminum

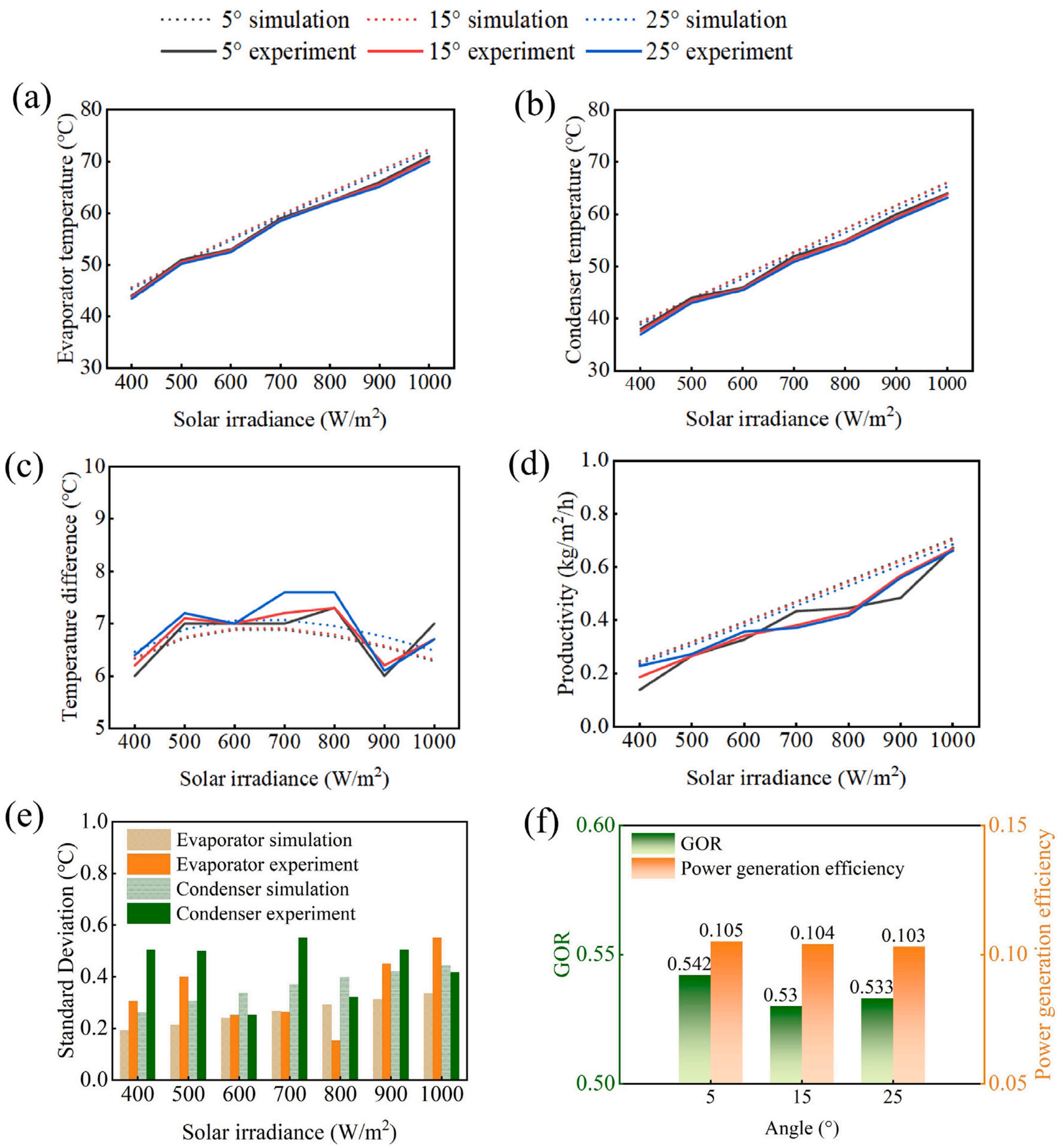

Fig. 11. Effect of inclination angle (5°, 15°, 25°) on system performance under varying irradiance (400–1000 W/m^2). (a) Evaporator center temperatures; (b) condenser center temperatures; (c) evaporator–condenser temperature difference; (d) freshwater productivity. In panels (a–d), dotted lines represent simulation results and solid lines represent experimental results. (e) Standard deviation of evaporator and condenser temperatures across the three angles under different irradiance level (orange bars: evaporator; green bars: condenser). (f) PV power generation efficiency (orange bars, left axis) and GOR (green bars, right axis) at the three inclination angles under 1 sun irradiance.

Table 6
Performance comparison between fixed-orientation and sun-tracking operational modes. Both tests were conducted under similar weather conditions (ambient temperatures 18–25°C, partly cloudy, wind speed 0–6 m/s). Noontime values correspond to the values during 11:00–15:00 and daily values correspond to the values during 10:00–17:00.

Parameters	Fixed (22° South)	Sun-tracking	Improvement
Temperature performance			
Noontime evaporator temperature	43.5–58.4°C (3 h > 55°C)	All over 55°C	Extended duration
Noontime condenser temperature	29.9–55.1°C	36.7–46.7°C	–
Production performance			
Peak productivity	0.412 kg/m^2/h	0.465 kg/m^2/h	+12.9%
Daily freshwater yield	1.73 kg/m^2	2.66 kg/m^2	+53.8%
Peak GOR (POA as denominator)	0.642	0.646	+0.62%
Daily GOR (POA as denominator)	0.348	0.366	+5%
Daily IEF	1.02	1.26	+23.5%

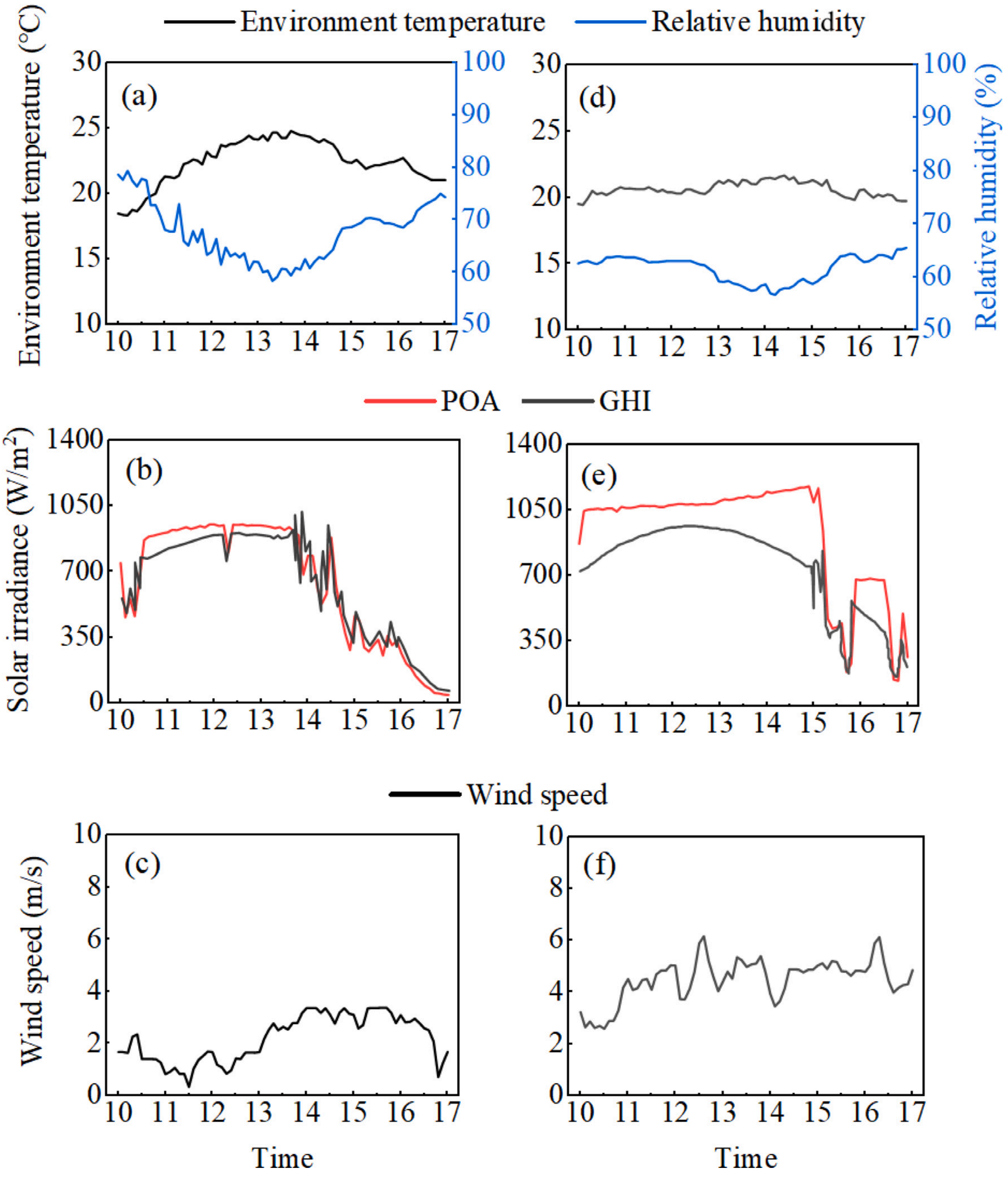

Fig. 12. Environmental conditions during fixed-orientation and sun-tracking experiments. Left column (fixed-orientation mode) and right column (sun-tracking mode). (a & d) ambient temperature (black line) and relative humidity (blue line); (b & e) POA (red line) and GHI (black line) solar irradiance; (c & f) wind speed. All data recorded from 10:00–17:00.

increased the contact angle to 107.9° ± 1.2°, a 300% improvement over the untreated surface that substantially improved droplet mobility. Combined with sea–island fiber drainage guides and dual symmetric bottom outlets, the condenser achieved a freshwater collection efficiency of 70% during short-term testing and 90% during long-term testing.

Indoor experiments investigated the effect of inclination angle on system performance when the irradiance level incident on the device is maintained. Despite a slight decrease in temperature at steeper angles, freshwater productivity remained constant at 0.65 kg/m^2/h across the 5–25° range under 1000 W/m^2 irradiance. This is because the faster brine flow at steeper angles reduces residence time on the heated surface, offsetting any evaporation gains. The inclination angle, therefore, has no significant effect on freshwater productivity, and the device should, in practice, be oriented at the location-specific optimum angle for electricity generation.

Outdoor testing at Hong Kong Polytechnic University validated real-world performance. At a fixed 22° south-facing orientation, the system produced 1.73 kg/m^2 of freshwater daily, with a peak productivity of 0.412 kg/m^2/h. Evaporator temperatures ranged from 51.7–58.4°C at noontime. Manual sun-tracking increased daily water production by 53.8% to 2.66 kg/m^2, while sustaining evaporator temperatures above

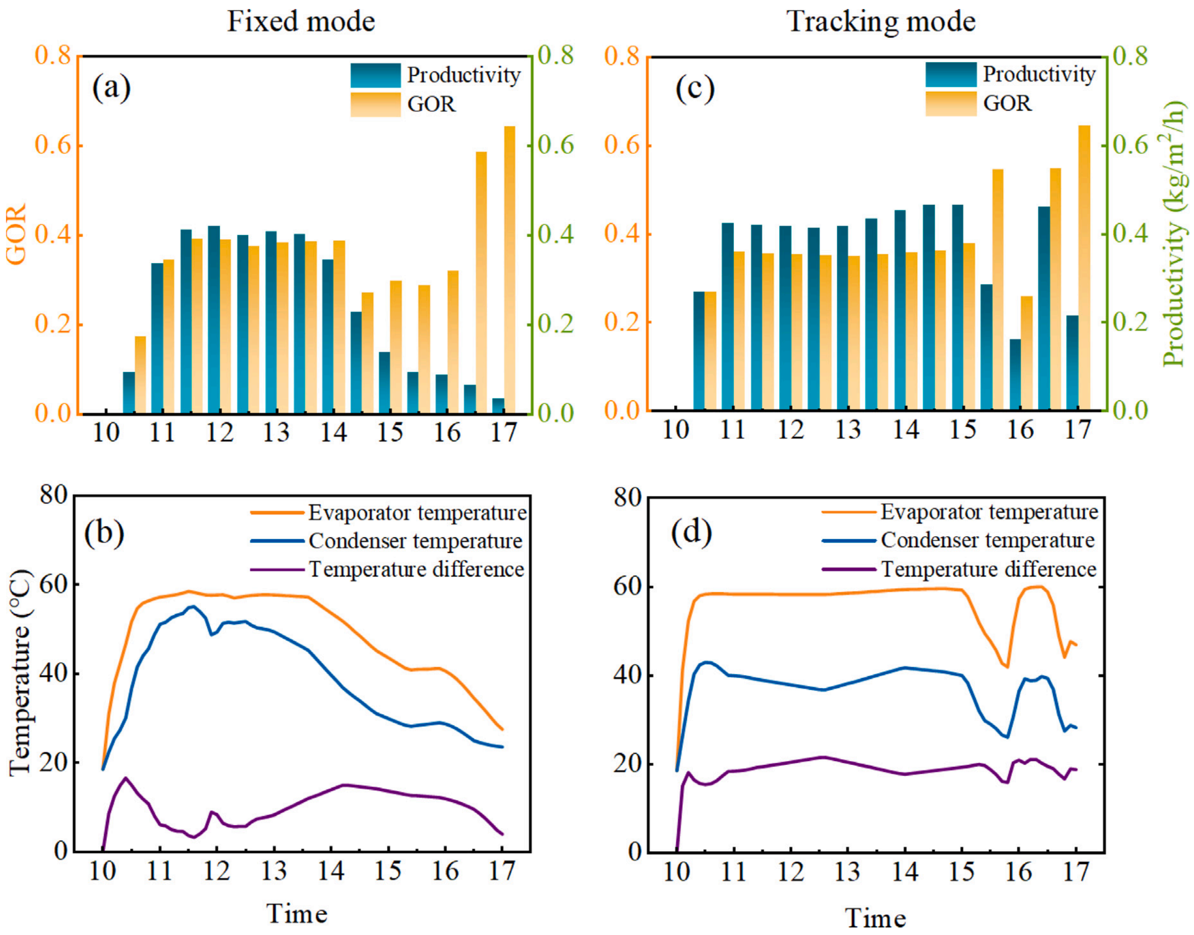

Fig. 13. Outdoor performance comparison between fixed-orientation and sun-tracking operational modes. Left column (fixed-orientation mode) and Right column (sun-tracking mode). (a & c) GOR (orange bars, left axis) and freshwater productivity (green bars, right axis) in 30-minute intervals; (b & d) evaporator temperature (orange line), condenser temperature (blue line) and evaporator–condenser temperature (purple line). All data recorded from 10:00–17:00.

55°C for over five hours, thereby improving received irradiance, GOR, and productivity stability.

In summary, the integrated design eliminates external cooling pipes and condensers while maintaining full cogeneration functionality. By recovering waste heat that would otherwise be abandoned, the system demonstrates practical cascade energy utilization from a single solar input. This approach is well-suited to distributed applications in water-scarce, sun-rich regions where both electricity and freshwater are needed, but infrastructure is limited, offering a practical and scalable pathway toward the effective utilization of the full solar energy spectrum.

CRediT authorship contribution statement

Lihao Yuan: Conceptualization, Methodology, Writing – original draft. **Zhiheng Qiu:** Writing – original draft, Methodology, Software, Validation, Formal analysis. **Omar AlAli:** Writing – review & editing, Formal analysis. **Ronghui Qi:** Writing – review & editing. **Mengying Li:** Conceptualization, Methodology, Supervision, Funding acquisition, Writing – review & editing.

Declaration of Generative AI and AI-assisted technologies in the writing process

During the preparation of this work, the authors used GPT-4 in order to improve language and readability. After using this tool, the authors reviewed and edited the content as needed and took full responsibility for the content of the publication.

Declaration of competing interest

The authors declare that they have no known competing financial interests or personal relationships that could have appeared to influence the work reported in this paper.

Acknowledgments

The authors gratefully acknowledge the substantial support from the Hong Kong University Grants Committee (UGC) under project number C6003-22Y, and the support from Hong Kong Polytechnic University, Hong Kong under project number P0055995. The authors extend their gratitude to Dr. Lu Wang for his invaluable technical support in setting up the experimental systems.

Data availability

Data will be made available on request.

References

[1] G. Di Baldassarre, N. Wanders, A. AghaKouchak, L. Kuil, S. Rangecroft, T.I. Veldkamp, M. Garcia, P.R. van Oel, K. Breinl, A.F. Van Loon, Water shortages worsened by reservoir effects, Nat. Sustain. 1 (11) (2018) 617–622.
[2] M.O. Mohie El Din, A.M. Moussa, Water management in Egypt for facing the future challenges, J. Adv. Res. 7 (3) (2016) 403–412.

[3] E.J. Okampo, N. Nwulu, Optimisation of renewable energy powered reverse osmosis desalination systems: A state-of-the-art review, Renew. Sustain. Energy Rev. 140 (2021) 110712.

[4] Z. Xu, X. Cai, X. Yin, M. Su, Y. Wu, Z. Yang, Is water shortage risk decreased at the expense of deteriorating water quality in a large water supply reservoir? Water Res. 165 (2019) 114984.

[5] International Energy Agency, International Renewable Energy Agency, United Nations Statistics Division, World Bank, World Health Organization, Tracking SDG7: The energy progress report 2023, ISBN: 978-1-4648-1983-5, 2023, URL https://trackingSDG7.esmap.org/.

[6] Intergovernmental Panel on Climate Change (IPCC), Climate change 2014: Mitigation of climate change, in: Contribution of Working Group III To the Fifth Assessment Report of the Intergovernmental Panel on Climate Change, 2014, http://dx.doi.org/10.1017/CBO9781107415416.

[7] G. Masson, E. Bosch, A.V. Rechem, M. de l'Epine, Snapshot 2024, Tech. rep., International Energy Agency Photovoltaic Power Systems Programme (IEA PVPS), 2024.

[8] M.S. Tahir, X. Dong, M.M. Khan, I.U. Rehman, Thermal management of photovoltaic systems: a comprehensive review of cooling strategies, Sol. Energy 299 (2025) 113811.

[9] A. Amelia, Y. Irwan, W. Leow, M. Irwanto, I. Safwati, M. Zhafarina, Investigation of the effect temperature on photovoltaic (PV) panel output performance, Int. J. Adv. Sci. Eng. Inf. Technol 6 (5) (2016) 682–688.

[10] A.K. Tiwari, K. Chatterjee, S. Agrawal, G.K. Singh, A comprehensive review of photovoltaic-thermal (PVT) technology: Performance evaluation and contemporary development, Energy Rep. 10 (2023) 2655–2679.

[11] A.M. Manokar, D.P. Winston, A. Kabeel, S. El-Agouz, R. Sathyamurthy, T. Arunkumar, B. Madhu, A. Ahsan, Integrated PV/T solar still-a mini-review, Desalination 435 (2018) 259–267.

[12] S.A. Rahman, R.K. Varma, T. Vanderheide, Generalised model of a photovoltaic panel, IET Renew. Power Gener. 8 (3) (2014) 217–229.

[13] P.V. Kumar, A. Kumar, O. Prakash, A.K. Kaviti, Solar stills system design: A review, Renew. Sustain. Energy Rev. 51 (2015) 153–181.

[14] O. Badran, H. Al-Tahaineh, The effect of coupling a flat-plate collector on the solar still productivity, Desalination 183 (1–3) (2005) 137–142.

[15] A.A. Badran, I.A. Al-Hallaq, I.A.E. Salman, M.Z. Odat, A solar still augmented with a flat-plate collector, Desalination 172 (3) (2005) 227–234.

[16] D.P. Winston, P. Pounraj, A.M. Manokar, R. Sathyamurthy, A. Kabeel, et al., Experimental investigation on hybrid PV/T active solar still with effective heating and cover cooling method, Desalination 435 (2018) 140–151.

[17] M. Naroei, F. Sarhaddi, F. Sobhnamayan, Efficiency of a photovoltaic thermal stepped solar still: experimental and numerical analysis, Desalination 441 (2018) 87–95.

[18] Z. Zhou, Y. Zhang, W. Liu, C. Gui, L. Huang, H. Huang, K. Fan, Y. Huang, Y. Gong, A. Chen, et al., Photovoltaic cooling and atmospheric water harvesting using a hygroscopic hydrogel, Desalination 583 (2024) 117685.

[19] Y. Su, Y. Lu, R. Gu, W. Wu, X. Yu, S. Cheng, Synergistic photovoltaic cooling and water-resource recovery enabled by a composite evaporation gel, Desalination (2025) 119565.

[20] W. Wang, S. Aleid, Y. Shi, C. Zhang, R. Li, M. Wu, S. Zhuo, P. Wang, Integrated solar-driven PV cooling and seawater desalination with zero liquid discharge, Joule 5 (7) (2021) 1873–1887.

[21] W. Wang, Y. Shi, C. Zhang, S. Hong, L. Shi, J. Chang, R. Li, Y. Jin, C. Ong, S. Zhuo, et al., Simultaneous production of fresh water and electricity via multistage solar photovoltaic membrane distillation, Nat. Commun. 10 (1) (2019) 3012.

[22] Y. Qiu, M. Zhang, Y. Wang, X. Guo, Z. Shi, H. Wang, X. Yu, Modeling and performance evaluation of a new multi-physical coupled system of photovoltaic-thermoelectric-interfacial evaporation, Energy Convers. Manage. 333 (2025) 119810.

[23] M. Zhou, L. Zhang, S. Tao, R. Li, Y. Wang, Recent research advances in efficient solar-driven interfacial evaporation, Chem. Eng. J. (2024) 151157.

[24] M.A. Razakov, Convective heat transfer coefficient modelling in laboratiry tests of photovoltaic solar modules efficiency, in: 2024 6th International Youth Conference on Radio Electronics, Electrical and Power Engineering, REEPE, IEEE, 2024, pp. 1–5.

[25] S. Zheng, J. Yu, R. Li, B. Zhou, Z. Xu, Contactless solar distiller with enhanced water yield via porous absorber, Desalination (2025) 119683.

[26] M. Kaviany, Principles of Heat Transfer in Porous Media, Springer Science & Business Media, 2012.

[27] W.M. Haynes, CRC Handbook of Chemistry and Physics, CRC Press, 2016.

[28] J. Darkwa, J. Calautit, D. Du, G. Kokogianakis, A numerical and experimental analysis of an integrated TEG-PCM power enhancement system for photovoltaic cells, Appl. Energy 248 (2019) 688–701.